17th Australasian Fluid Mechanics Conference
Auckland, New Zealand
5-9 December 2010

Aerothermodynamics of Hypersonic Shock Wave Boundary Layer Interactions

N. R. Deepak, S. L. Gai and A. J. Neely

School of Engineering & IT
High Speed Flow Group
UNSW, Australian Defence Force Academy
Canberra 2600, Australia

Abstract

Hypersonic laminar flow past a 24° compression corner has been numerically investigated using computational fluid dynamics. The flow conditions were: specific total enthalpy of $h_o \approx 19MJ/kg$, $R_e \approx 3.1 \times 10^5 1/m$ and a Mach number of $M_\infty \approx 7.5$. A grid independence study has been carried out to estimate the sensitivity of heat flux and pressure in the strong interaction regions of the flow. The CFD investigation of perfect gas has also been extended to study the influence of real-gas effects such as thermal and chemical nonequilibrium using Park's two-temperature model with finite-rate chemistry. The CFD results are compared with the available experimental data.

Introduction

Hypersonic flow past a compression corner is a typical problem of shock wave/boundary layer interaction (SWBLI). The importance of SWBLI on aerothermodynamic characteristics has led to its extensive investigation due to its relevance in the design of hypersonic space vehicles. While the compression corner problem appears to be a simplified geometric configuration, it is analogous to a number of generic regions of separated flow on a space vehicle. In high enthalpy hypersonic flow, the total energy content is sufficiently high enough to cause changes in the internal distribution of energy levels within the gas. This leads to molecular excitation that eventually induces chemical reactions via dissociation and ionisation. This is the thermo-chemical, non-equilibrium behaviour of the flow. Understanding SWBLI under such a scenario is therefore necessary for the reliable design of space vehicles.

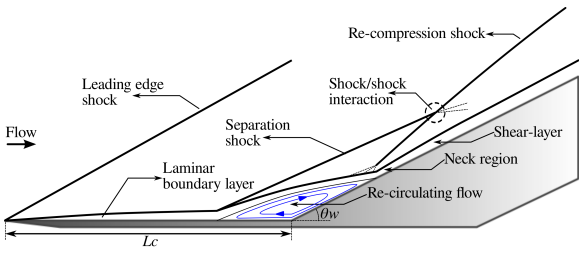

Figure 1: Flow schematic over a 2D compression corner

The laminar flow over a compression corner as shown in Figure 1 is characterised by boundary layer over the flat plate with a leading edge shock. With of the presence of the corner, a shock wave forms and interacts with the boundary layer. If the corner angle (θ_w) is large enough, then the boundary layer separates forming a separation bubble with recirculating flow. A separation shock in turn forms at the location where the boundary layer separates. Depending upon the Mach number, the leading edge shock may interact with the separation or reattachment shock. Downstream from the corner, the separated shear-layer reattaches to the surface. When this occurs, the thickness of the shear-layer is reduced and the flow turns towards the surface forming a neck, which is also shown in Figure 1. The compression waves thus generated coalesce to form a reattachment shock. Downstream of reattachment the shear-layer grows and the flow becomes parallel to the surface. The separated shock may interact with the recompression shock forming a shock/shock interaction with the emergence of a slip line.

Geometric configuration & Flow conditions

A sharp leading edge flat-plate of length ($L_c = 85\ mm$) followed by a compression corner with a ramp angle (θ_w) of 24° is considered here under laminar flow high enthalpy conditions. The down stream ramp has a length of 95 *mm*. The flow is assumed to be two-dimensional. Experimental investigation [7] for this comparison was initially carried out at the T3 shock-tunnel facility with a specific total enthalpy of 19 MJ/kg and with a unit Reynolds number of $3.10 \times 10^5\ 1/m$ and $M_\infty \approx 7.5$. Air was used as the test gas. The CFD calculations have therefore been performed at these flow conditions. Table 1 summarises the freestream conditions used for this investigation.

U_∞ m/s	T_∞ K	p_∞ KPa	ρ_∞ kg/m^3	T_w/T_o -	γ -
5470	1160	0.99	2.60×10^{-3}	0.035	1.45

Table 1: Freestream conditions (Condition *B* [7]).

The test gas composition evaluated [7] for condition *B* through non-equilibrium analysis is given in Table 2.

Species	N_2	O_2	N	O	NO
Mass fraction	0.750	0.06	0.001	0.159	0.03

Table 2: Freestream species concentration

Computational Modelling

The two-dimensional flow field of interest was modelled using a multi-block Navier-Stokes solver, Eilmer-3 [6]. Eilmer-3 is a time-dependent, compressible, viscous, three-dimensional solver capable of solving laminar, turbulent and chemically reactive flows. Eilmer-3 operates on finite-volume approach, where the discritization occurs at the center of each control volume. A modified van Albada limiter and MUSCL (Monotone Upstream-centered Schemes for Conservation Laws) reconstruction scheme [1] are used to obtain second-order spatial accuracy. To calculate the mass, momentum and energy flux across the cells, the advection upwind splitting method combining difference and vector splitting (AUSMDV) [11] method is used. AUSMDV has robust shock-capturing capabilities, where the discontinuities are captured with high resolution and is particularly suitable for solving finite-rate chemical reactions. The carbuncle phenomena typically encountered during multi-dimensional shock capturing is treated here with shock-fix technique [11]. Eilmer has capability to solve the multi-block grids utilising multiple CPU through Message Passing

Interface (MPI) library. Therefore, the CFD calculations were accordingly performed on multiple CPUs.

The grid independence study was performed using the assumption of perfect gas [3, 4, 10]. The grid independence study using the perfect gas assumption is justified because with the real gas effects, the only difference will be that it takes longer time for grid convergence. This is because with the real gas, the gas is treated as a mixture of thermally perfect gases. Air was used as the test gas with single species assumption and the thermodynamic behaviour was modelled as colorically perfect with a constant ratio of specific heats. In this case, the transport properties were evaluated using the Sutherland formulation. Real gas effects such as chemical and thermal nonequilibrium phenomena in the flow filed were additionally investigated using the Park's [9] kinetic mechanism. The finite-rate chemistry for air with five species was computed for the dissociation and recombination reactions, ignoring the effects of ionisation. The thermal nonequilibrium effects were computed using the two-temperature model of Park [9]. Details of finite rate reactions are given in Table 3 and reaction rates were calculated from the Arrhenius coefficients given in Park [9].

5-Neutral dissociation-recombination reactions
$N_2 + M \rightleftharpoons N + N + M$
$O_2 + M \rightleftharpoons O + O + M$
$NO + M \rightleftharpoons N + O + M$
$NO + O \rightleftharpoons O_2 + N$
$N_2 + O \rightleftharpoons NO + N$

Table 3: Finite-rate chemical reactions for high temperature air

For the real-gas computations, the gas is treated as a mixture of thermally perfect gases, where C_p and C_v are functions of temperature. The energy exchange between vibrational and translational modes of the molecules were evaluated using the Landua-Teller equation and vibrational relaxation time was then estimated using the Millikan and White empirical correlation [9]. The vibrational energy was finally calculated using the harmonic oscillator model in a Boltzmann distribution given at the vibrational temperature (T_{ve}). Transport properties of the species mixture were then calculated using the method adopted by NASA's CEA program [5] that utilises interaction potential between each of the species for estimation. The finite-rate chemical reactions were modelled as a set of ordinary differential equations using a alpha-QSS method [6]. Diffusion velocities were modelled using a modified a Ficks Law [6].

A CGNS multi-block structured grid was developed for this problem using the commercial package, ICEM-CFD. The upstream flat-plate and the wedge surfaces are modelled as cold wall with a fixed wall temperature of T_w=300K. The inlet boundaries are specified with uniform supersonic velocities and the supersonic outlet is specified at the trailing edge of the model. Initialisation of the CFD simulation was performed with zero velocity and a pressure of 50 Pa, similar to the experimental conditions at $t = 0s$. The flow was simulated in a time-accurate manner, until the flow variables converged to steady conditions. The grid independence study is carried out for this configuration and follows the approach adapted by Deepak et al. [2] for high enthalpy separated flows. Non-dimensional heat flux (Stanton number) variation is known to provide a sensitive test [2] for CFD solution and hence is used here as a criteria along with surface pressure and skin-friction. However, only Stanton number sensitivity is presented in Figure 2. Here, the wetted surface (s), is normalised with the upstream flat-plate length (L_c), such that $s/L_c = 1$ represents the corner location. The Stanton number number was evaluated as

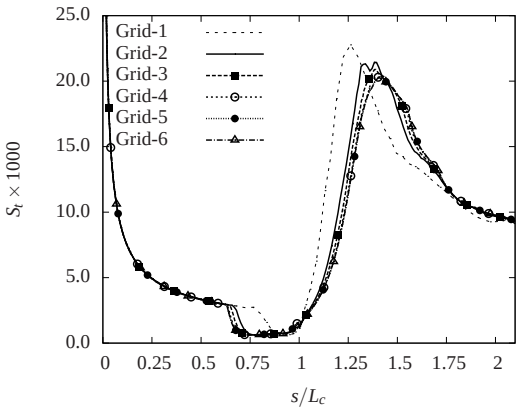

Figure 2: Stanton number distribution for various grids

$S_t = q_w/[\rho_e u_e(h_r - h_w)]$. where, q_w is the surface heat flux and h_r is the recovery enthalpy evaluated as $h_r = h_e + \sqrt{Pr}u_e^2/2$. The subscript e refers to the condition that exists at the edge of the boundary layer.

As can be noted from Figure 2, in the region $0 \leq s/L_c \leq 0.625$ not much variation in heat flux is noted. However, as the heat flux reduces due to separation ($0.625 \leq s/L_c \leq 0.75$), changes are evident. Grid-1 severely under estimates the separation location. With further grid refinement, separation size appears to increase. Only after Grid-5, no change in the value of the Stanton number at separation is seen. Immediately after separation, within the recirculation region, not much differences between various grids can be noticed, except Grid-1. This suggests that, although heat flux may be insensitive with sufficiently refined grids in the separated region, adequate grid resolution is still required to predict proper scale of separation and its location. Downstream of the reattachment ($s/L_c \approx 1.2$), significant variations can be noted in the close vicinity of peak heat flux location. While, Grid-1 can be seen to over estimate the heat flux until it reaches a peak value, further downstream it under estimates in comparison to other grids. With more refinement, a gradual reduction in heat flux occurs as well as the location of the peak on the wedge surface. This indicates that both reattachment and peak heat flux location are highly grid dependent.

Beyond $s/L_c \approx 1.75$ in Figure 2, the region where heat flux gradually reduces, not much grid sensitivity is seen similar to what is seen upstream of separation. Nevertheless, only beyond Grid-5, heat flux does not vary with refinement in regions of separation/reattachment and up to the trailing edge. Hence, all other computations were carried out using Grid-5. Grid-5 comprises of 570 nodes in x and 102 nodes in y directions respectively, contributing to 58140 nodes in total. The first node from the wall surfaces (Δy) was at a distance of 20 $\times 10^{-6} m$ (20 μm). It has been shown by Deepak et al. [2] that Δy of this order is required for proper heat flux estimation in high enthalpy separated flows. Since these numerical experiments were time-accurate, it was found that 280 μs was required for the flow quantities to become completely established. For a perfect gas analysis, this was ~130 hours of computational time on 8 core Xeon CPUs. Figure 3 shows schematically the grid distribution for Grid-2.

Results & Discussions

In Figure 4, the Stanton number (S_t) distribution obtained through CFD is compared with the experiments as well as the CFD data of Olejniczak and Candler [8]. Olejniczak and Candler [8] carried out two-dimensional CFD simulations using Park's [9] two-temperature model including chemistry for the

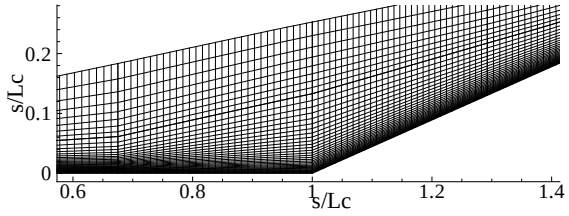

Figure 3: Structured grid distribution for Grid-2

same geometric configuration and flow condition as presently investigated. The data of Olejniczak and Candler [8] taken here for comparison was obtained on their finest grid comprised of (1024 $\times$ 1024). With respect to the present simulation results, we present two sets of CFD data, one under the assumption of perfect gas (PG) and the other assuming thermo-chemical non-equilibrium real-gas (RG). The reason for comparing the experimental data with CFD simulations assuming both perfect gas and real gas was because Mallinson et al. [7] found that for the experimental data considered here, the real gas effects were negligible.

As can be see from Figure 4 the distribution of heat-flux over the initial length of the flat-plate is a result of attached boundary layer growth and the leading edge shock. In this region, not much difference can be seen between the present CFD data, although it slightly over predicts the experimental data. However, Olejniczak and Candler [8] results closely match the experimental values. After $s/L_c \approx 0.625$, where the heat flux reduction is seen, separation occurs. Here, number of differences can be seen. The perfect-gas data seem to over predict the separation size, while the real-gas prediction appears to be closer to the experimental value. This is also in close agreement with the Olejniczak and Candler [8] CFD data. Within the recirculation region upstream of the corner, all the CFD data compare well with experiments.

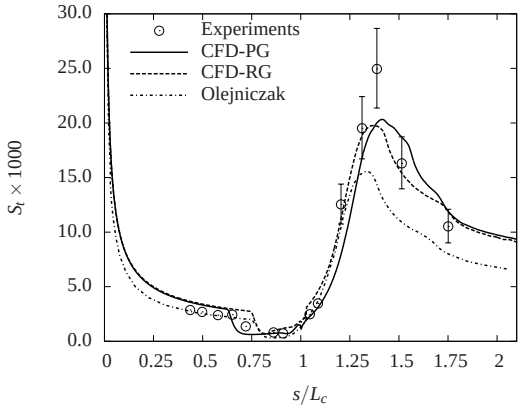

Figure 4: Stanton number distributions

Downstream from the corner after the separated shear layer reattaches to the plate, some interesting trends are seen. As the neck region forms (see Figure 1), the thickness of the shear layer is reduced increasing the heat flux to a peak value. Close to the vicinity of this peak, reattachment occurs. Due to the reduction in shear-layer thickness, the temperature gradients become steep causing high surface heat flux. This is quite clearly seen in both CFD data and experiments. However, some significant differences are seen. Firstly, none of the CFD data matches the experimental peak heat flux location which is at $s/L_c \approx 1.37$. They all seem to under predict the peak heat flux by a considerable margin. Nevertheless, the present CFD real-gas result matches most of the other experimental points over the wedge surface. In contrast, the data of Olejniczak and Candler [8] severely under predicts, except in the immediate region past the corner location. A possible explanation for this may be that Olejniczak and Candler [8] found that their computations with finer grid (1024 $\times$ 1024) were much lower than the experimental data than the solution with the grid (512 $\times$ 512). They do not offer any explanation for this apparent anomaly. Suffice to say at this stage that the present solution with Grid-5 and real gas assumption does predict results closer to the experimental data.

The under prediction of the peak heat flux with respect to experiments suggests that a transition in the separated shear layer might have occurred or that it is a three-dimensional effect. Since all the CFD simulations have been performed assuming laminar flow and two-dimensional conditions, these effects could not be investigated. Downstream of reattachment, the shear-layer grows and the flow becomes parallel to the surface causing a decrease in heat-flux to the surface.

Figure 5 shows the normalised pressure distribution in comparison with experiments and also Olejniczak and Candler [8] data. On the flat plate far upstream of the corner, the CFD results from the three sets are in close agreement and indicate a typical distribution of pressure due the boundary layer growth. The real-gas CFD results cannot be distinguished from the perfect gas data. It should however be noted that there are no experimental data to compare in this far upstream region. A pressure increase and plateau can be seen to occur which is a consequence of adverse pressure gradient which leads to separation. Based on the location of increase in surface pressure and decrease in heat flux from the real gas model, the separation location may be considered to occur at $s/L_c \approx 0.75$. This value also seems to match with Olejniczak and Candler [8] data. The pressure inflection in perfect gas prediction occurs slightly ahead of that of the real-gas predictions. A similar trend was also noted with the reduction in heat flux over this region. This illustrates that the scale of separated region is over predicted with the perfect-gas model. The CFD data from Olejniczak and Candler [8] almost matches the present CFD real-gas data in the separated region. The two sets of data also compare quite well with experiments.

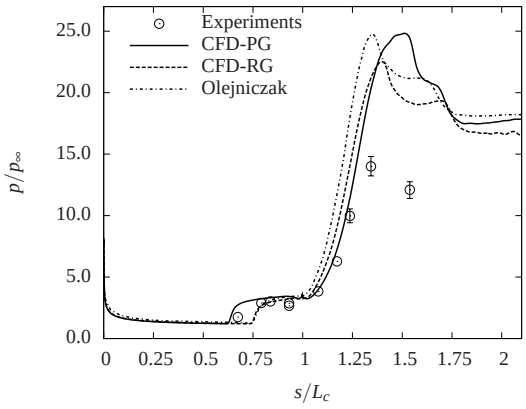

Figure 5: Normalised pressure (p/p_∞) distributions

Downstream from the corner, the CFD results from all the three sets more or less equally over predict the peak experimental values. However, some agreement with experiments is seen immediately downstream of the corner with present CFD results. The Olejniczak and Candler [8] data on the other hand show much more deviation from the experiments. The location

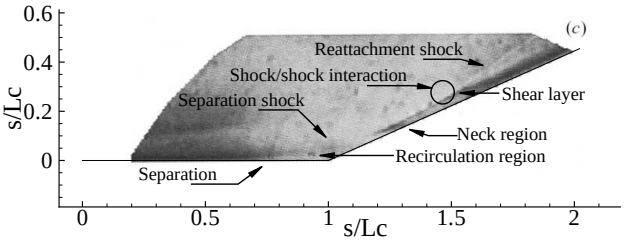

(a) Experimental infinite fringe

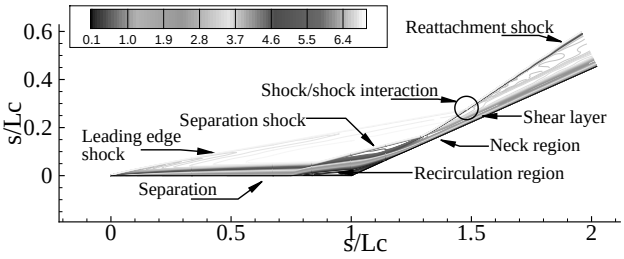

(b) Computed Mach contour (Real gas)

Figure 6: Experimental and computational visualisation

of peak pressure indicating the shear layer reattachment to the plate matches the peak heat flux location. Beyond this location, the present real-gas computation shows a much reduced pressure in comparison to both perfect-gas and Olejniczak and Candler [8] data, but no where close to the experiments. The reduced pressures in the case of experiments may, as noted earlier, indicate transition or three-dimensional effects. However, three-dimensional effects would seem unlikely because, in the experiments, the model was fitted with side skirts.

Figure 6 shows an infinite fringe flow visualisation obtained from the experiment compared with the CFD real-gas data. The flow features from the fringe diagram have been delineated from the photographic images so that some inaccuracies in the measurements are possible. Here, the Mach contour in grey scale is shown to compare the flow features. As can be seen, the boundary layer thickness predicted over the flat plate region matches the fringe pattern reasonably well. The location of separation and the recirculation region in general are also in close agreement with the visualised image. The other features that are in close agreement are the separation shock, reattachment shock and the shear layer downstream. This indicates that the separation size and the reattachment locations are correctly modelled. In addition, the shock/shock interaction effect from separation and the reattachment shocks is also is also correctly modelled and matches the experimental image.

Conclusions

CFD simulations have been carried out for the flow past a two-dimensional compression corner in high enthalpy hypersonic flow. Detailed grid independence study indicates the sensitive areas in the flow field where adequate grid resolution is required. Effects of real-gas phenomena have been considered through modelling thermo-chemical nonequilibrium simulation. The simulated data and experimental comparison appear to show that CFD can reasonably predict the laminar SWBLI in the separated region close to the corner. Nevertheless, some significant differences were noted over the downstream wedge surface, particularly in the location and magnitude of the peak heat flux and pressure and the subsequent distribution of heat flux and pressure. The study has shown that separation, reattachment and recirculation regions are affected by real gas effects.

Acknowledgements

The authors would like to express their sincere thanks to the following people. Dr. Peter Jacobs of the University of Queensland for allowing us to use his Eilmer-3 solver. Daniel Potter of University of Queensland and Dr. Rowan Gollan of NASA Langley Research Center for their support in explaining various intricacies in Eilmer-3 and its usability.

References

[1] Anderson, W. K. and Thomas, J. L., A comparison of finite volume flux vector splittings for the euler equations, *AIAA*, **24**, 1986, 1453–1460.

[2] Deepak, N. R., Gai, S. L. and Neely, A. J., A computational study of high enthalpy flow over a rearward facing step, in *48th AIAA Aerospace Sciences Meeting Including the New Horizons Forum and Aerospace Exposition in Orlando, Florida, 4-7 Jan 2010*, 2010, number 2010-444.

[3] Druguet, M.-C., Ben-Dor, G. and Zeitoun, D., The interaction of supersonic and hypersonic flows with a double cone: comparison between inviscid, viscous, perfect and real gas model simulations, in *26th International Symposium on Shock Waves, Gottingen, Germany*, 2007, volume 2.

[4] Gnoffo, P. A., Cfd validation studies for hypersonic flow prediction, in *39th AIAA Aerospace Sciences Meeting & Exhibit, 8-11 Jan 2001, Reno, NV*, 2001, number 2001-1025.

[5] Gordon, S. and McBride, B. J., Computer program for calculation of complex chemical equilibrium compositions and applications: I analysis, Technical Report Reference Publication 1311, NASA, 1994.

[6] Jacobs, P. A. and Gollan, R. J., The eilmer3 code, Technical Report Report 2008/07, Department of Mechanical Engineering, University of Queensland, Brisbane, 2010.

[7] Mallinson, S. G., Gai, S. L. and Mudford, N. R., The interaction of a shock wave with a laminar boundary layer at a compression corner in high-enthalpy flows including real gas effects, *Journal of Fluid Mechanics*, **342**, 1997, 1–35.

[8] Olejniczak, J. and Candler, G. V., Computation of hypersonic shock interaction flow fields, in *7th AIAA/ASME Joint Thermophysics and Heat Transfer Conferene*, AIAA, 1998.

[9] Park, C., Review of chemical-kinetic problems of future nasa missions, i: Earth entries, *Journal of Thermophysics and Heat Transfer*, **7**, 1993, 385–398.

[10] Simeonides, G. and Haase, W., Experimental and computational investigations of hypersonic flow about compression ramps, *Journal of Fluid Mechanics*, **283**, 1995, 17–42.

[11] Wada, Y. and Liou, M. S., A flux splitting scheme with high-resolution and robustness for discontinuities, in *Aerospace Sciences Meeting and Exhibit, 32nd, Reno, NV, Jan 10-13, 1994*, 1994, number AIAA-1994-83.